Image Sharpness Assessment Based on Local Phase Coherence

Rania Hassen, Zhou Wang, *Senior Member, IEEE*, and Magdy M. A. Salama, *Fellow, IEEE*

***Abstract*— Sharpness is an important determinant in visual assessment of image quality. The human visual system is able to effortlessly detect blur and evaluate sharpness of visual images, but the underlying mechanism is not fully understood. Existing blur/sharpness evaluation algorithms are mostly based on edge width, local gradient, or energy reduction of global/local high frequency content. Here we understand the subject from a different perspective, where sharpness is identified as strong local phase coherence (LPC) near distinctive image features evaluated in the complex wavelet transform domain. Previous LPC computation is restricted to be applied to complex coefficients spread in three consecutive dyadic scales in the scale-space. Here we propose a flexible framework that allows for LPC computation in arbitrary fractional scales. We then develop a new sharpness assessment algorithm without referencing the original image. We use four subject-rated publicly available image databases to test the proposed algorithm, which demonstrates competitive performance when compared with state-of-the-art algorithms.**[1]

***Index Terms*— Complex wavelet transform, image blur, image quality assessment (IQA), image sharpness, local phase coherence (LPC), phase congruency.**

I. Introduction

QUALITY assessment of visual images is of fundamental importance in modern multimedia systems, where various types of distortions are introduced during acquisition, storage, transmission, processing and display of images. Since humans are the ultimate consumers in most applications, the most dependable way to assess visual images is to solicit opinions from human observers. However, subjective evaluation is extremely costly and time-consuming, and is often difficult to implement in real applications, especially when real-time quality control is desired. What are really needed are efficient objective image quality assessment (IQA) approaches that can well predict human evaluations of image quality [1].

The most common IQA approaches measure the similarity or fidelity between the distorted image and a reference image that is assumed to be perfect-quality and distortion-free. Examples of such full-reference (FR) IQA algorithms include peak signal-to-noise-ratio (PSNR), the structural similarity (SSIM) index [2], and visual information fidelity [3]. Reduced-reference (RR) IQA provides an alternative approach, where partial information (in the form of features extracted from the image) about the reference image is available in evaluating the quality of the distorted image [1]. However, in a large number of applications such as image denoising, deblurring and enhancement, the reference image is unavailable, and thus FR and RR approaches are not applicable. Therefore, in these scenarios, no-reference (NR) IQA that does not require any access to the reference image is highly desirable [1].

In this paper, we are concerned about NR assessment of image sharpness, which is one of the most determining factors in human judgement of image quality. Sharpness is closely associated with blur, which is the most common type of distortion that impairs visual sharpness. In practice, blur may occur during image acquisition, e.g., due to atmospheric turbulence, camera motion, or out-of-focus of the optical system. It may also be a side effect of certain image processing operations such as compression and denoising. Interestingly, the human visual system (HVS) has a remarkable capability to detect image blur without seeing the original image, but the underlying mechanisms are not well understood.

In the literature, several types of computational models have been proposed to account for the perception of blur. The first type of models examine the power spectrum of an image in global/local frequency transformations such as the Fourier transform [4]. This is motivated by the fact that blur is often created through low pass filtering, which smooths images and reduces their high frequency energy. As a result, the power spectrum of a blurred image falls faster than the original sharp natural image, whose power spectrum falloff often obeys a power law [4]. Following the framework, a sharpness/blur measure may be implemented by evaluating high-frequency energy [5], by computing an HVS-weighted summation of normalized power spectrum [6], by counting near-zero high frequency discrete cosine transform (DCT) coefficients [7], or by calculating the ratio between high and low frequency energy [8].

The second class of models focus on edges and associate blur with edge width. Edge detection algorithms are first employed to find edges and edge widths are estimated along either horizontal/vertical [9] or local gradient direction [10], followed by a blur measure computed as the average edge width over all edges detected [9]. In [11], the edge detection and edge width approaches were incorporated with a novel concept of just noticeable blur (JNB), which is a perceptual

Manuscript received March 28, 2012; revised January 21, 2013; accepted February 23, 2013. Date of publication March 7, 2013; date of current version May 22, 2013. Partial preliminary results of this work were presented at 2009 IEEE International Conference on Image Processing (Cairo, Egypt) and 2011 International Conference on Image Analysis and Recognition (Burnaby, BC, Canada). The associate editor coordinating the review of this manuscript and approving it for publication was Prof. Alex C. Kot.

The authors are with the Department of Electrical and Computer Engineering, University of Waterloo, Waterloo, ON N2L 3G1, Canada (e-mail: rhassen@uwaterloo.ca; zhouwang@ieee.org; m.salama@ece.uwaterloo.ca).

Color versions of one or more of the figures in this paper are available online at http://ieeexplore.ieee.org.

Digital Object Identifier 10.1109/TIP.2013.2251643

[1] A MATLAB code of the proposed algorithm is available online at https://ece.uwaterloo.ca/ z70wang/research/lpcsi/.

model indicating the probability of detecting a blur distortion by human eyes. It was shown that the JNB value is a function of local contrast and psychophysical experiments were carried out to calibrate the model [12]. The JNB method was further refined in a cumulative probability of blur detection (CPBD) measure [13], which is based on a probabilistic framework on the sensitivity of human blur perception at different contrasts. The CPBD measure achieves state-of-the-art performance when tested with multiple image databases [13].

The third category of blur prediction models are based on statistics on the distribution of pixel intensities or transform coefficients. Pixel intensity statistical methods are based on the hypothesis that sharper images have larger variance or higher entropy in their intensity values [14], [15]. Kurtosis of 2D DCT coefficient distribution has also been found to be a useful measure to characterize image sharpness [16]. In [16], such a kurtosis measure is combined with an edge profile based method, leading to an effective image sharpness measure. Total variation (TV) between adjacent pixel values in an image region has been employed as a measure of local sharpness in a probabilistic framework [17].

The fourth type of models employ local gradient measures based on the observation that the strength of local gradient is sensitive to image blur. In [18], singular value decomposition is applied to groups of gradient vectors computed within local patches. The two resulting singular values provide useful measures of gradient strength along the dominant direction and its perpendicular direction, respectively. A sharpness measure H is then defined by making use of the dominant singular value as well as prior knowledge about the noise variance. In [19], a normalized form that accounts for the relative gradient strength between the dominant and its perpendicular directions was proposed. This results in an improved sharpness measure Q that was employed for automatic parameter selection of image denoising algorithms.

All aforementioned four types of blur/sharpness models are well-motivated and are shown to be effective in capturing certain aspects about the impact of blur on perceived sharpness, and they have achieved notable success when tested using a number of subject-rated databases. On the other hand, these methods are often limited by the complication of the large variations between real-world images in terms of information content and complexity. For example, it was pointed out that individual images show significant variability in their amplitude spectra both in shape and in the speed of falloff [20]. For another example, the overall gradient strength of an image not only depends on the degree of blur, but is also largely affected by the amount of sharp detail presented in the original source image. A useful idea is to combine the merits of different blur/sharpness models. For example, the recently proposed S_3 algorithm [21] combines TV-based spatial sharpness measure and block-wise power spectral falloff features and achieves significantly improved performance.

In this paper, we examine image sharpness/blur from a different and complementary perspective. The idea is originated from the notion of local phase coherence (LPC) [22], which reveals that the phases of complex wavelet coefficients constitute a highly predictable pattern in the scale space in the vicinity of sharp image features. LPC may be considered as a generalization of the phase congruency concept [23], which describes the phase alignment across scales at the exact location of distinctive image features. Detailed discussions regarding the differences between LPC and phase congruency are given in Section II. It was shown that the LPC structure is disrupted by image blur [22], which motivates us to develop an LPC strength measure and use it as an image sharpness estimator.

The main contributions of this paper are as follows. First, we introduce a novel framework to compute LPC using samples arbitrarily extracted from the scale-space. This has significant advantages over previous methods [22], [24], where LPC computation was limited to three dyadic scales only. The proposed computation framework is more flexible, and more importantly, can be made more space- and scale-localized, and thus reduces interference from nearby image features. Second, we propose an efficient LPC evaluation algorithm that largely simplifies the LPC computation, making it easily applicable in practical applications. Third, based on the relationship between LPC and perceptual blur/sharpness, we develop a sharpness estimator and test it using four publicly-available subject-rated image databases. Competitive performance in comparison with state-of-the-art algorithms is achieved with low computational cost.

II. Local Phase Coherence

The concept of LPC was first introduced in [22], which describes the alignment of local phase patterns in the scale-space in the vicinity of distinctive sharp image features. It may be interpreted as an extension of the phase congruency relationship [23], which stands for the phase alignment of global/local phases across scales at the exact location of distinctive image features. Given a signal $f(x)$ created from a feature signal $f_0(x)$ but located near position x_0, i.e. $f(x) = f_0(x - x_0)$, a general family of complex wavelet transform may be written as

$$\begin{aligned} F(s, p) &= \int_{-\infty}^{\infty} f(x) w_{s,p}^{*}(x) dx \\ &= \left[f(x) * \frac{1}{\sqrt{s}} g\left(\frac{x}{s}\right) e^{J\omega_c x/s} \right]_{x=p} \end{aligned} \tag{1}$$

where $s \in R^{+}$ is the scale factor, $p \in R$ is the translation factor, and the family of wavelets $w_{s,p}(x)$ are derived from a scaled and shifted mother wavelet $w(x) = g(x)e^{j\omega_c x}$ by

$$\begin{aligned} w_{s,p}(x) &= \frac{1}{\sqrt{s}} w\left(\frac{x-p}{s}\right) \\ &= \frac{1}{\sqrt{s}} g\left(\frac{x-p}{s}\right) e^{J\omega_c (x-p)/s} \end{aligned} \tag{2}$$

where ω_c is the center frequency of the modulated band-pass filter, and $g(x)$ is a slowly varying, non-negative and symmetric envelop function. For example, when $g(x)$ has the shape of a Gaussian, $w_{s,p}(x)$ constitutes a family of Gabor wavelets. However, the derivation below also applies to other options of $g(x)$.

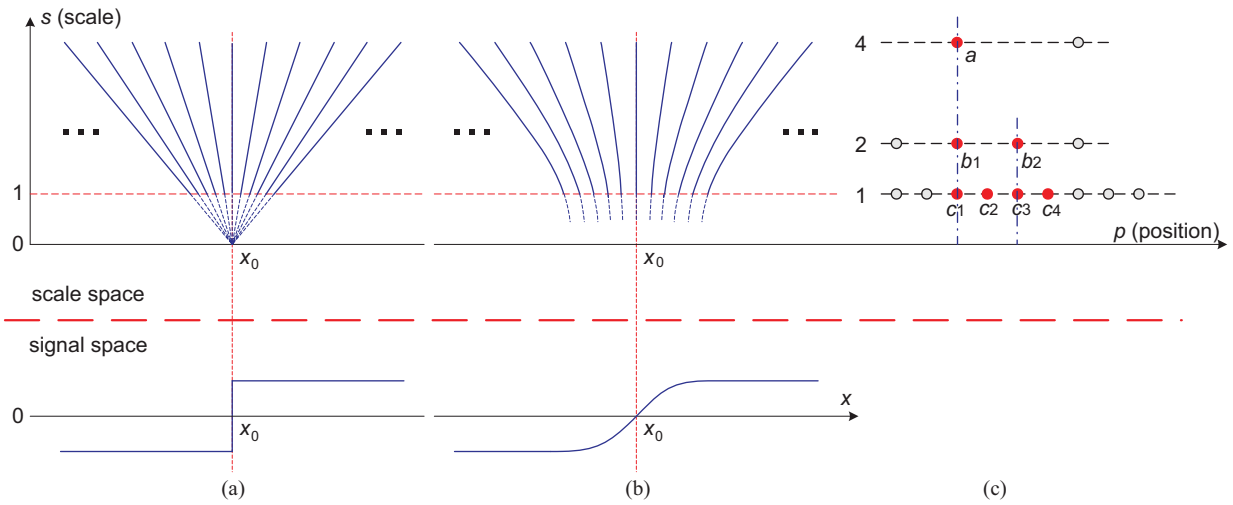

Fig. 1. Local phase coherence structure near (a) sharp step edge and (b) blurred step edge, where the equal-phase contours in the scale space are shown. The phase congruency relationship corresponds to the central vertical contours at position x_0 in both (a) and (b), but does not describe the phase structures in the vicinity of x_0. (c) Positions of discrete sampling across three consecutive dyadic scales in the scale space.

Using the convolution theorem, and the shifting and scaling properties of the Fourier transform, we can derive:

$$F(s,\,p)=\frac{1}{2\pi\sqrt{s}}\int_{-\infty}^{\infty}F_0\left(\frac{\omega}{s}\right)G(\omega-\omega_c)\,e^{j\omega(p-x_0)/s}d\omega \tag{3}$$

where $F(\omega)$, $F_0(\omega)$ and $G(\omega)$ are the Fourier transforms of $f(x)$, $f_0(x)$ and $g(x)$, respectively. The phase of $F(s,\,p)$ depends on the nature of $F_0(\omega)$. If $F_0(\omega)$ is scale invariant, meaning that

$$F_0(\omega/s)=K(s)F_0(\omega) \tag{4}$$

where $K(s)$ is a real function of only s, but independent of ω, then

$$F(s,\,p)=\frac{K(s)}{2\pi\sqrt{s}}\int_{-\infty}^{\infty}F_0\,(\omega)\,G(\omega-\omega_c)\,e^{j\omega(p-x_0)/s}d\omega. \tag{5}$$

This suggests a predictable structure of $F(s,\,p)$ from $F(1,\,p)$ given by

$$F(s,\,p)=\frac{K(s)}{K(1)\sqrt{s}}\,F\left(1,x_0+\frac{p-x_0}{s}\right). \tag{6}$$

Since both $K(s)$ and s are real, we obtain the following phase relationship of $F(s,\,p)$:

$$\Phi(F(s,\,p))=\Phi\left(F\left(1,x_0+\frac{p-x_0}{s}\right)\right). \tag{7}$$

This result indicates that there is a strong phase coherence relationship across scale and space, where equal phase contours in the $(s,\,p)$ plane form straight lines that converge exactly at the location of the feature x_0, as illustrated in Fig. 1(a). These straight lines are defined by $x_0+(p-x_0)/s=D$, where D is a constant. The phase congruency relationship constitutes a subset of LPC by predicting the phases in the same way for the center vertical line ($p=x_0$) only. Note that the derivation of the LPC phase pattern is based on the assumption that f_0 is a scale invariant signal, which turns out to be true for distinctive sharp features (such as an isolated impulse or a step edge in a 1D signal, or an edge, a line, or an isolated impulse in a 2D image). This gives another property that distinguishes the LPC relationship with phase congruency, which does not require the scale-invariance feature and holds for other types of features also (e.g., a blurred edge). This is illustrated in Fig. 1(b), where blur does not change the central vertical contour ($p=x_0$), but distorts the general LPC patten away from the center.

It has been shown that if the LPC relationship is satisfied at a spatial location, then the phase of a wavelet coefficient can be predicted using the phases of its neighboring coefficients in the scale-space [22]. An example is shown in Fig. 1(c), where the finest scale coefficients c_i for $i=1,2,3,4$ can be predicted from their coarser scale neighbors a, b_1 and b_2. For example,

$$\hat{\Phi}(c_1)=-2\Phi(a)+3\Phi(b_1) \tag{8}$$

where $\hat{\Phi}(c_1)$ denotes the prediction of the true phase $\Phi(c_1)$.

Conversely, the prediction accuracy (i.e., the closeness between $\Phi(c_1)$ and $\hat{\Phi}(c_1)$) can be used as a local measure of the strength of the LPC relationship. In our previous work [24]–[26], a method was proposed to compute a spatial LPC map in the complex wavelet transform domain based on the complex version of the steerable pyramid decomposition [27]. Following a 3-scale, multi-orientation steerable pyramid transform, the phases of the finest scale coefficients are predicted using their corresponding parent and grandparent coefficients using an LPC-based phase predictor (such as (8)). At each spatial location, an LPC strength measure is then defined as

$$P_i=\frac{\sum_j\left|c_{ij}\right|\cos\left(\Phi\left(\left\{c_{ij}\right\}\right)-\widehat{\Phi}\left(\left\{c_{ij}\right\}\right)\right)}{\sum_j\left|c_{ij}\right|} \tag{9}$$

where $\Phi\left(\left\{c_{ij}\right\}\right)$ and $\widehat{\Phi}\left(\left\{c_{ij}\right\}\right)$ are the true and predicted phases of the i-th coefficient in the j-th orientation, respectively. This measure achieves the maximal value of unity when the phase prediction (and thus LPC relationship) is perfect. This is expected to occur in the vicinity of distinctive sharp image features. The measure is weighted by the magnitudes

of the coefficients over orientations, so that the orientations that contain more energy are given higher weights. Such an LPC measure had been employed in image registration [25], fusion [26], and sharpness assessment [24] applications.

III. Proposed Methods

Since the LPC relationship holds at sharp image features only, it was conjectured that the visual perception of blur may be interpreted as a loss of LPC and the conjecture is partially supported by local phase statistics of sharp and blurred natural images [22]. This is in clear contrast when compared with traditional views about image blur, which was often understood as the reduction of high frequency energy, the reduction of contrast, or the expansion of edge width. If the conjecture about the relationship between LPC and perceptual image sharpness/blur holds, then the strength of LPC may be used as a measure of image sharpness. This idea has been exploited in our preliminary study [24] with some level of success. However, the method to compute LPC in all previous studies has strong limitations. Specifically, the computation is applicable to three spatially neighboring complex wavelet coefficients spread in three consecutive dyadic scales only, where the widths of the wavelet filters expand by factors of 1, 2, and 4, respectively, from the finest to the coarsest scales. In practice, such a large expansion of the coarsest scale filter is often problematic because nearby image features may interfere with the responses of these coefficients (but may or may not affect the finer scale coefficients). As a result, the LPC relationship is often corrupted even if the local image feature is sharp. Consequently, it is highly desirable to develop more flexible (preferably more space- and scale-localized) LPC computation methods.

A. Local Phase Patterns at Sharp Features

To develop a new method to compute LPC, we would need to closely examine the phase patterns at sharp features. Like in [22], we analyze the LPC relationship in 1D and the results can be directly extended to 2D. In 1D, the most common sharp features are impulses and ideal step edges. In the case of an impulse $f_0(x) = A\delta(x)$, where A is a non-zero constant and $\delta(x)$ is the impulse function. The Fourier transform of $f_0(x)$ is $F_0(\omega) = A$ for all ω, and thus $F_0(\omega/s) = A$ and $K(s)$ in (4) equals unity. Substitute this into (5), we have

$$\begin{aligned} F(s,p) &= \frac{1}{2\pi\sqrt{s}} \int_{-\infty}^{\infty} A\, G(\omega-\omega_c)\, e^{j\omega(p-x_0)/s} d\omega \\ &= \frac{A}{\sqrt{s}}\, g\left(\frac{p-x_0}{s}\right) e^{j\omega_c \frac{p-x_0}{s}}. \end{aligned} \tag{10}$$

The derivation above is based on the fact that the RHS of the first row constitutes the inverse Fourier transform of $\frac{A}{\sqrt{s}} G(\omega-\omega_c)$ evaluated at $(p-x_0)/s$. The phase of $F(s,p)$ is then

$$\Phi(F(s,p)) = \begin{cases} \frac{\omega_c(p-x_0)}{s} & \text{when} A > 0 \\ \frac{\omega_c(p-x_0)}{s} + \pi & \text{when} A < 0. \end{cases} \tag{11}$$

In the case of an ideal step edge, $f_0(x) = B\left[u(x) - \frac{1}{2}\right]$, where B is a non-zero constant and $u(x)$ is the step function. The Fourier transform of $f_0(x)$ is $F_0(\omega) = \frac{B}{j\omega}$ and $F_0\left(\frac{\omega}{s}\right) = \frac{Bs}{j\omega} = sF_0(\omega)$. Thus $K(s) = s$ in (4). Substitute this into (5), we have

$$F(s,p) = \frac{B\sqrt{s}}{2\pi} \int_{-\infty}^{\infty} \frac{G(\omega-\omega_c)}{j\omega} e^{j\omega(p-x_0)/s} d\omega \tag{12}$$

where the RHS constitutes the inverse Fourier transform of $\frac{B\sqrt{s}G(\omega-\omega_c)}{j\omega}$ evaluated at $(p-x_0)/s$. Based on the integration property of Fourier transform, we obtain

$$\begin{aligned} F(s,p) &= B\sqrt{s} \int_{-\infty}^{\frac{p-x_0}{s}} g(x)\, e^{j\omega_c x} dx \\ &= \frac{B\sqrt{s}}{j\omega_c} \left[g(x) e^{j\omega_c x} \Big|_{-\infty}^{\frac{p-x_0}{s}} - \int_{-\infty}^{\frac{p-x_0}{s}} g'(x)\, e^{j\omega_c x} dx \right]. \end{aligned} \tag{13}$$

Since $g(x)$ is a slowly varying function localized near $x = 0$, we have $g(-\infty) = 0$ and $g'(x) \approx 0$. Therefore,

$$F(s,p) \approx \frac{B\sqrt{s}}{j\omega_c}\, g\left(\frac{p-x_0}{s}\right) e^{j\omega_c \frac{p-x_0}{s}}. \tag{14}$$

The phase is then computed as

$$\Phi(F(s,p)) \approx \begin{cases} \frac{\omega_c(p-x_0)}{s} - \frac{\pi}{2} & \text{when } B > 0 \\ \frac{\omega_c(p-x_0)}{s} + \frac{\pi}{2} & \text{when } B < 0. \end{cases} \tag{15}$$

Combining (11) and (15), we obtain a general LPC relationship given by

$$\Phi(F(s,p)) \approx \hat{\Phi}(s,p) \equiv \frac{\omega_c(p-x_0)}{s} + \frac{k\pi}{2} \tag{16}$$

where k is an integer depending on the nature of the sharp feature. Specifically, it equals 0, 2, -1, and 1 for positive impulse, negative impulse, ideal ascending step edge, and ideal descending step edge, respectively.

B. LPC Evaluation from Arbitrary Samples in Scale-Space

The general relationship in (16) provides a model of the phase pattern in the vicinity of a sharp image feature. Given the phases of N sample coefficients arbitrarily extracted from $F(s,p)$ near x_0 and their corresponding predictions

$$\boldsymbol{\Phi} = \begin{bmatrix} \Phi[F(s_1,p_1)] \\ \Phi[F(s_2,p_2)] \\ \vdots \\ \Phi[F(s_N,p_N)] \end{bmatrix}, \quad \hat{\boldsymbol{\Phi}}_{x_0,k} = \begin{bmatrix} \hat{\Phi}(s_1,p_1) \\ \hat{\Phi}(s_2,p_2) \\ \vdots \\ \hat{\Phi}(s_N,p_N) \end{bmatrix} \tag{17}$$

we can quantify the strength of LPC by assessing the closeness between the true phases of these coefficients and their optimal model predictions

$$S_{\text{LPC}} = \max_{\{x_0,k\}} S(\boldsymbol{\Phi}, \hat{\boldsymbol{\Phi}}_{x_0,k}) \tag{18}$$

where $S(.,.)$ is a similarity measure between the true and predicted phase samples given in vector form as in (17).

The most straightforward way to define the similarity function S is to make it monotonically decreasing with the squared error between the vectors. For example, we may define

$$S(\boldsymbol{\Phi}, \hat{\boldsymbol{\Phi}}_{x_0,k}) = \frac{1}{1 + \alpha \left\| \boldsymbol{\Phi} - \hat{\boldsymbol{\Phi}}_{x_0,k} \right\|^2} \tag{19}$$

where α is a positive constant, and this similarity function is bounded between 0 and 1. As a result, solving the optimization problem in (18) is equivalent to solving a least square optimization problem. For each given value of k (for $k = -1,\ 0,\ 1,\ 2$), the optimal value x_0 in (18) can be found in closed-form, and the overall optimization problem can then be resolved by picking the value k and its corresponding x_0 that lead to the minimal squared error. Although this method is simple and computationally efficient, the solutions turn out to be erroneous and unreliable in our experiment. The reason is because phase variables are not normal scalar quantities but are angular variables that have the 2π wrap-around effect (for example, an error of 2π is equivalent to 0 error for an angular variable but is significant in the linear scale).

To overcome the wrap-around effect as well as the ambiguity between different types of features (that correspond to different k values), we used a different method in [28], which corresponds to defining a similarity function as

$$S(\mathbf{\Phi}, \hat{\mathbf{\Phi}}_{x_0,k}) = \frac{1}{N}\sum_{i=1}^{N}\cos\{4\Phi[F(s_i,\, p_i)] - 4\hat{\Phi}(s_i,\, p_i)\}. \quad (20)$$

This similarity function is bounded between -1 and 1. Notice that the factor 4 here makes the last term in (16) a multiplier of 2π. This factor, when combined with the use of the cosine function, eliminates both the wrap-around effect and the ambiguity between different features. Although this similarity definition is conceptually elegant, it makes the optimization problem in (18) difficult to solve, and in general, no closed-form solution can be found. In practice, we have to resort to numerical optimization tools, which often lead to extremely high computational cost (as in [28]), especially when this approach is applied to 2D images, where the optimization procedure needs to be carried out at every location in the image.

C. Efficient LPC Evaluation Algorithm

Given the difficulties in the LPC evaluation methods described above, our focus below will be on practical algorithms that lead to efficient assessment of LPC. It is worth noting that the general formulation laid out in (18) allows for arbitrary selections of samples (in terms of both the number and positions of the samples) of $F(s, p)$ in the scale-space. In practice, this is unlikely and unnecessary. Motivated by the method used in [22], we may pick a set of samples at specific positions and scales in the scale-space, so that the LPC computation can be largely simplified. In particular, if we can find a set of samples $\hat{\mathbf{\Phi}}$, together with a corresponding set of weights $\mathbf{w} = [w_1, w_2, \cdots, w_N]^T$, such that

$$\mathbf{w}^T\,\hat{\mathbf{\Phi}} = 0 \quad (21)$$

then we may define a simple measure of LPC strength by

$$S_{\mathrm{LPC}} = \cos\left(\mathbf{w}^T\,\mathbf{\Phi}\right). \quad (22)$$

The value of this LPC measure is bounded between -1 and 1, and the maximal value is achieved when $\mathbf{w}^T\,\mathbf{\Phi} = 0$, which is consistent with the phase relationship defined in (21).

To provide an example (that may lead to a practically useful LPC measure), let us assume that we extract N samples in the scale-space that are aligned at the same position p (which may not be aligned with the feature position x_0) but at different scales. Substitute (16) into (21), we obtain

$$\omega_c(p - x_0)\left(\sum_{i=1}^{N}\frac{w_i}{s_i}\right) + \frac{k\pi}{2}\left(\sum_{i=1}^{N} w_i\right) = 0. \quad (23)$$

In order for this to be true for all possible values of ω_c, p, x_0 and k, we would need the following simultaneous equations to be true

$$\begin{cases}\sum\limits_{i=1}^{N} w_i = 0\\ \sum\limits_{i=1}^{N}(w_i/s_i) = 0.\end{cases} \quad (24)$$

Without loss of generality, we assume $w_1 = 1$. This results in $N - 1$ unknowns $(w_2,\ w_3,\ \cdots,\ w_N)$ with two equations. In the case that $N = 3$, the solutions are unique and are given by

$$\begin{cases} w_1 = 1\\ w_2 = \frac{s_2(s_3 - s_1)}{s_1(s_2 - s_3)}\\ w_3 = \frac{s_3(s_2 - s_1)}{s_1(s_3 - s_2)}.\end{cases} \quad (25)$$

When $N > 3$, we can solve for a least square weight energy solution under the constraints of (24). Using a Lagrange multiplier approach, we define the following energy function

$$E = \sum_{i=1}^{N} w_i^2 + \lambda_1\left(\sum_{i=1}^{N} w_i\right) + \lambda_2\left(\sum_{i=1}^{N}\frac{w_i}{s_i}\right) \quad (26)$$

where λ_1 and λ_2 are the Lagrange multipliers. Taking derivative of E with respect to λ_1, λ_2 and w_i for $i = 1, 2, \cdots, N$ and setting them to zero, we obtain a linear system of equations

$$\mathbf{A}\mathbf{w}^* = \mathbf{b} \quad (27)$$

where

$$\mathbf{A} = \begin{bmatrix} 1 & 0 & \cdots & 0 & 1/2 & 1/2s_2\\ 0 & 1 & \cdots & 0 & 1/2 & 1/2s_3\\ \vdots & \vdots & \ddots & \vdots & \vdots & \vdots\\ 0 & 0 & \cdots & 1 & 1/2 & 1/2s_N\\ 1 & 1 & \cdots & 1 & 0 & 0\\ 1/s_2 & 1/s_3 & \cdots & 1/s_N & 0 & 0\end{bmatrix}$$

$$\mathbf{w}^* = \begin{bmatrix} w_2 & w_3 & \cdots & w_N & \lambda_1 & \lambda_2\end{bmatrix}^T$$

$$\mathbf{b} = \begin{bmatrix} 0 & 0 & \cdots & 0 & -1 & -1/s_1\end{bmatrix}^T. \quad (28)$$

We can then solve for the weights by

$$\mathbf{w}^* = \mathbf{A}^{-1}\mathbf{b}. \quad (29)$$

In practice, one would likely to choose s_1 to be the finest scale ($s_1 = 1$) for maximal localization, and choose the other s_i values to be evenly spaced in either linear or logarithm scale. For example, in $N = 3$ case,

$$\begin{bmatrix} s_1\\ s_2\\ s_3\end{bmatrix} = \begin{bmatrix} 1\\ 1 + d\\ 1 + 2d\end{bmatrix} \quad \text{or} \quad \begin{bmatrix} s_1\\ s_2\\ s_3\end{bmatrix} = \begin{bmatrix} 1\\ r\\ r^2\end{bmatrix}. \quad (30)$$

TABLE I
WEIGHT SOLUTIONS FOR THREE SCALES

	s_1	s_2	s_3	w_1	w_2	w_3
	1	$1+d$	$1+2d$	1	$-2(1+d)$	$1+2d$
$d=1/4$	1	5/4	3/2	1	$-5/2$	3/2
$d=1/2$	1	3/2	2	1	-3	2
$d=1$	1	2	3	1	-4	3
$d=3/2$	1	5/2	4	1	-5	4
$d=2$	1	3	5	1	-6	5
	1	r	r^2	1	$-(1+r)$	r
$r=5/4$	1	5/4	25/16	1	$-9/4$	5/4
$r=\sqrt{2}$	1	$\sqrt{2}$	2	1	$-1-\sqrt{2}$	$\sqrt{2}$
$r=\sqrt{3}$	1	$\sqrt{3}$	3	1	$-1-\sqrt{3}$	$\sqrt{3}$
$r=2$	1	2	4	1	-3	2
$r=\sqrt{5}$	1	$\sqrt{5}$	5	1	$-1-\sqrt{5}$	$\sqrt{5}$

The weight solutions of these two cases are computed as

$$\begin{bmatrix} w_1 \\ w_2 \\ w_3 \end{bmatrix} = \begin{bmatrix} 1 \\ -2(1+d) \\ 1+2d \end{bmatrix}$$

and

$$\begin{bmatrix} w_1 \\ w_2 \\ w_3 \end{bmatrix} = \begin{bmatrix} 1 \\ -(1+r) \\ r \end{bmatrix} \tag{31}$$

respectively. The solutions of the two cases for specific selections of d and r values are given in Table I. Interestingly, the previous LPC computation (8) becomes a special case that can be directly derived from the row for $r=2$ in Table I. In the cases of $N=4$ and $N=5$, the least square weight energy solutions for specific values of d and r are shown in Tables II and III, respectively.

TABLE II
WEIGHT SOLUTIONS FOR FOUR SCALES

	s_1	s_2	s_3	s_4	w_1	w_2	w_3	w_4
$d=1/3$	1	4/3	5/3	2	1	−1.9474	−0.1316	1.0789
$d=1/2$	1	3/2	2	5/2	1	−2.2347	−0.0408	1.2755
$d=2/3$	1	5/3	7/3	3	1	−2.5166	0.0464	1.4702
$d=1$	1	2	3	4	1	−3.0714	0.2143	1.8571
$d=2$	1	3	5	7	1	−4.7089	0.6962	3.0127
$r=2^{1/3}$	1	$2^{1/3}$	$2^{2/3}$	2	1	−1.5962	−0.2401	0.8363
$r=3^{1/3}$	1	$3^{1/3}$	$3^{2/3}$	3	1	−1.7828	−0.1683	0.9511
$r=4^{1/3}$	1	$4^{1/3}$	$4^{2/3}$	4	1	−1.9320	−0.1084	1.0404
$r=6^{1/3}$	1	$6^{1/3}$	$6^{2/3}$	6	1	−2.1686	−0.0097	1.1784
$r=2$	1	2	4	8	1	−2.3571	0.0714	1.2857

TABLE III
WEIGHT SOLUTIONS FOR FIVE SCALES

	s_1	s_2	s_3	s_4	s_5	w_1	w_2	w_3	w_4	w_5
$d=1/4$	1	5/4	3/2	7/4	2	1	−1.4477	−0.4827	0.2067	0.7237
$d=1/2$	1	3/2	2	5/2	3	1	−1.8458	−0.4581	0.3744	0.9295
$d=3/4$	1	7/4	5/2	13/4	4	1	−2.2252	−0.4350	0.5289	1.1314
$d=1$	1	2	3	4	5	1	−2.5957	−0.4137	0.6774	1.3320
$d=3/2$	1	5/2	4	11/2	7	1	−3.3237	−0.3745	0.9661	1.7321
$r=2^{1/4}$	1	$2^{1/4}$	$\sqrt{2}$	$2^{3/4}$	2	1	−1.1937	−0.4932	0.0958	0.5911
$r=3^{1/4}$	1	$3^{1/4}$	$\sqrt{3}$	$3^{3/4}$	3	1	−1.3271	−0.4818	0.1604	0.6484
$r=\sqrt{2}$	1	$\sqrt{2}$	2	$2\sqrt{2}$	4	1	−1.4314	−0.4698	0.2102	0.6910
$r=6^{1/4}$	1	$6^{1/4}$	$\sqrt{6}$	$6^{3/4}$	6	1	−1.5930	−0.4466	0.2858	0.7538
$r=8^{1/4}$	1	$8^{1/4}$	$2\sqrt{2}$	$8^{3/4}$	8	1	−1.7185	−0.4255	0.3434	0.8006

D. Image Sharpness Measure

Given an input image whose sharpness is to be evaluated, we first pass it through a series of N-scale M-orientation log-Gabor filters without any subsequent downsampling process. This results in MN "subbands" and there are MN complex coefficients at each spatial location across all orientations and all scales. Let c_{ijk} be the complex coefficient at the i-th scale, the j-th orientation and the k-th spatial location. Then at the j-th orientation and the k-th location, we can compute the LPC strength by

$$\begin{aligned} S_{\mathrm{LPC}}^{\{j,k\}} &= \cos(\mathbf{w}^T\,\mathbf{\Phi}_j) = \cos\left(\sum_{i=1}^{N} w_i\,\Phi\{c_{\mathrm{ijk}}\}\right) \\ &= \cos\left(\Phi\left\{\prod_{i=1}^{N} c_{\mathrm{ijk}}^{w_i}\right\}\right) \\ &= \frac{\Re\left\{\prod_{i=1}^{N} c_{\mathrm{ijk}}^{w_i}\right\}}{\left|\left\{\prod_{i=1}^{N} c_{\mathrm{ijk}}^{w_i}\right\}\right|} \end{aligned} \tag{32}$$

where $R\{\cdot\}$ denotes the real part of a complex number. This LPC strength measure is combined at each spatial location k by a weighted average across all orientations, where the weights are determined by the magnitude of the first (finest) scale coefficient $c_{1\mathrm{jk}}$, so that the orientations that contain more energy are given higher importance:

$$S_{\mathrm{LPC}}^{\{k\}} = \frac{\sum_{j=1}^{M} \left|c_{1\mathrm{jk}}\right| S_{\mathrm{LPC}}^{\{j,k\}}}{\sum_{j=1}^{M} \left|c_{1\mathrm{jk}}\right| + C} \tag{33}$$

where a constant C is added to avoid instability when the magnitudes of the coefficients are close to zero.

The collection of $S_{\mathrm{LPC}}^{\{k\}}$ at all locations constitutes a spatial LPC map. An example LPC map of a natural image of Fig. 2(a) is shown in Fig. 2(d). It can be observed that the local LPC strength measure responds strongly to sharp image structures around the sharp foreground region but weakly to the background out-of-focus regions. When the image is blurred as in Fig. 2(b), the strength of local LPC is reduced, reflecting the observation presented in Fig. 1, where it shows blur weakens the LPC relationship in the scale-space. When the image is severely blurred as in Fig. 2(c), the LPC relationship is completely disrupted, as shown in Fig. 2(f).

In order to provide an overall evaluation about the sharpness of the test image, we need to pool the LPC map into a single sharpness index. An effect in subjective sharpness assessment is that humans tend to make their judgment based on the sharpest region in the image [24]. For example, Fig. 4(a) is typically rated as a sharp image regardless of the out-of-focus background. This suggests that in pooling the LPC map, a mechanism is necessary to put more emphasis on the sharpest regions in the image. Here we propose a weighted averaging method based on ranked LPC values: Let

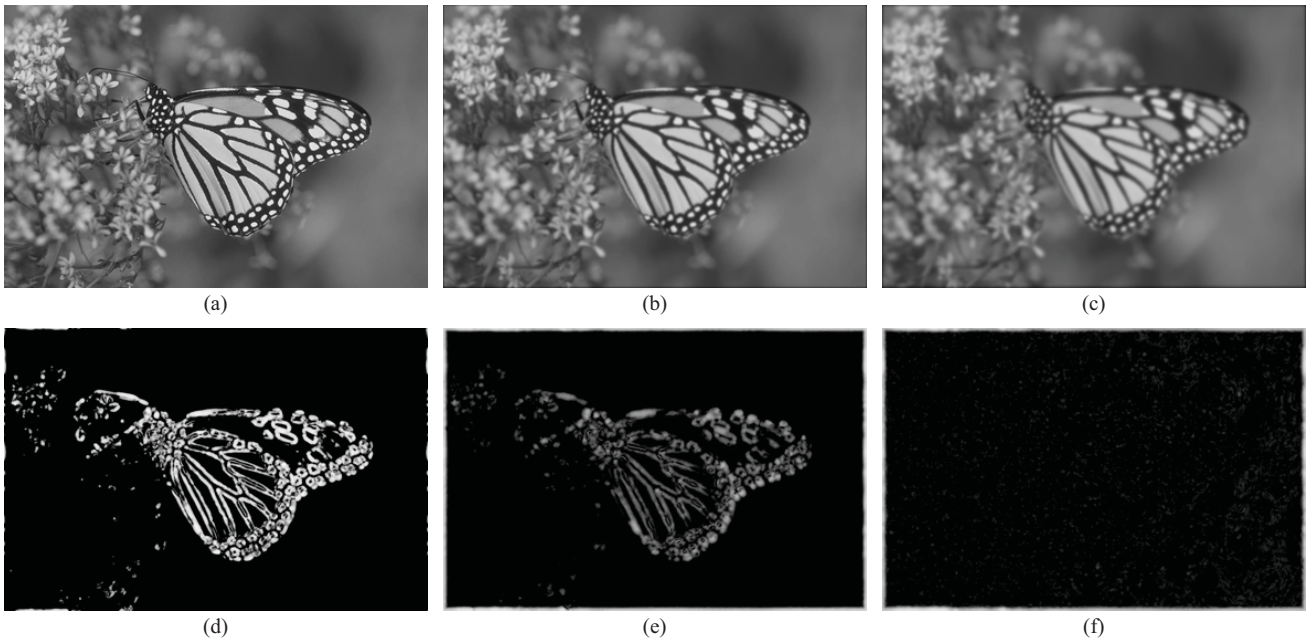

Fig. 2. (a) Original. (b) and (c) Gaussian blurred "Monarch" images at two blur levels, together with their corresponding LPC maps (d)–(f).

$S_{\text{LPC}}^{\{k\}}$ for $k = 1, 2, \ldots, K$ be a collection of LPC values extracted from the LPC map, and let $S_{\text{LPC}}^{\{(k)\}}$ for $k = 1, 2, \ldots, K$ denote the sorted LPC strength values such that $S_{\text{LPC}}^{\{(1)\}} \geq S_{\text{LPC}}^{\{(2)\}} \geq \cdots \geq S_{\text{LPC}}^{\{(K)\}}$. Then the overall LPC-based sharpness index (LPC-SI) is defined as

$$S_{\text{LPC}} = \frac{\sum_{k=1}^{K} u_k \, S_{\text{LPC}}^{\{(k)\}}}{\sum_{k=1}^{K} u_k} \tag{34}$$

where u_k is the weight assigned to the k-th ranked spatial LPC value and is computed as an exponentially decaying function given by

$$u_k = \exp\left[-\left(\frac{k-1}{K-1} \right) \Big/ \beta_k \right] \tag{35}$$

which gives a weight 1 to the highest LPC value and the decaying speed of the weights is controlled by the parameter β_k. In all the experimental results reported in the next section, the parameters are set as $M = 8$, $N = 3$, $s_1 = 1$, $s_2 = 3/2$, $s_3 = 2$, $C = 2$, and $\beta_k = 1e - 4$, respectively. These parameters are set empirically, but are found to be insensitive to the overall performance in our test with various blur image databases.

IV. Validation

A. No-Reference Sharpness Estimator

We test the performance of the proposed sharpness measure using four blur data sets obtained from four independent publicly available image databases.

1) The LIVE database [29] was developed at The University of Texas at Austin, where the blur data set contains 174 images including 145 blurred and 29 reference images. All images were rated by 20–25 subjects on a continuous linear scale divided into 5 regions, namely Bad, Poor, Fair, Good, and Excellent. For each image, the mean opinion score (MOS) and the standard deviation between subjective scores were recorded.
2) The Tampere Image Database 2008 (TID2008) [30] includes 100 Gaussian-blurred images obtained from 25 original images. Each image was evaluated by subjects from 0 to 9. The final MOS is obtained by averaging evaluated scores for a given image. Observers from three different countries (Italy, Finland and Ukraine) have performed two types of tests. The first test was conducted by direct evaluation of distorted images and the second by relative comparison between the quality of image pairs.
3) The Categorical Image Quality (CSIQ) database [31] was developed at Oklahoma State University, where the blur data set contains 150 Gaussian-blurred images created from 30 original images at four to five distortion levels. The images are subjectively rated base on a linear displacement of the images across four calibrated LCD monitors placed side by side with equal viewing distance to the observer. Ratings are reported in the form of Difference of MOS (DMOS) between the original and blurred images.
4) The IVC database [32] was developed at Ecole Polytechnique de l'Universite de Nantes. Four reference images have been distorted with 5 levels of Gaussian blur with a total of 20 blurred images. 15 subjects were asked to evaluate the distortion with respect to the original image on a five point scale. Subjective scores were reported in the form of MOS.

We compare the proposed LPC-SI method against seven existing NR sharpness measures, which include CPBD [13], JNBM [11], the H-metric [18], the Q-metric [19], S_3 [21], BRISQUE [33], [34], and BLIINDS-II [35], [36]. We have also included in our experiments two FR measures, PSNR and SSIM [2], which provide useful comparisons on the relative performance against the most widely used IQA measures. It should be noted that BRISQUE and BLIINDS-II are both

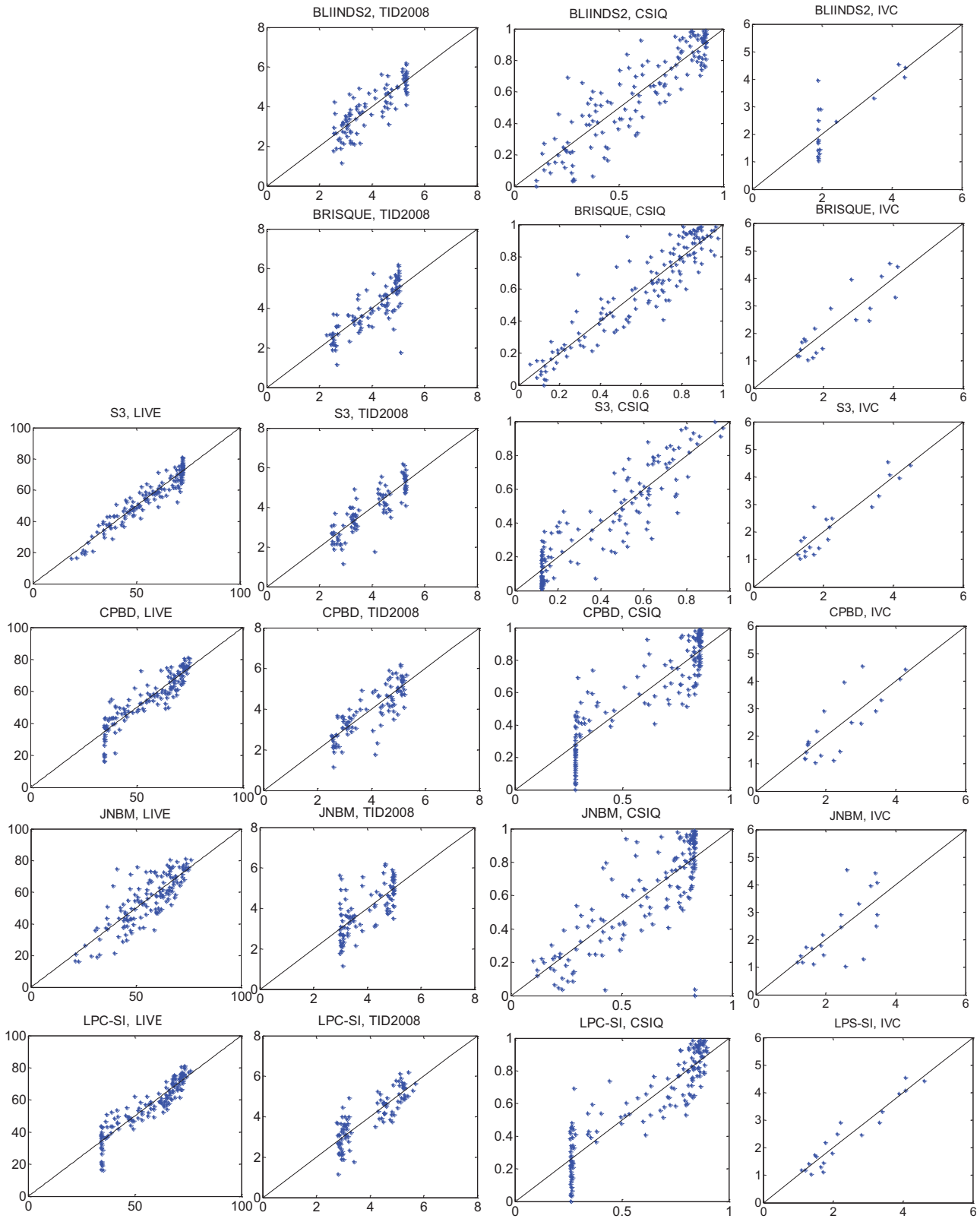

Fig. 3. Scatter plots between subjective and objective scores (after nonlinear mapping) of six blur metrics over four blur image databases. Top to bottom rows: BLIINDS-II [35], [36], BRISQUE [33], [34], S_3 [21], CPBD [13], JNBM [11], and the proposed LPC-SI measure; Left to right columns: LIVE, TID2008, CSIQ and IVC blur databases.

general-purpose NR IQA techniques that are not designed for assessing blur/sharpness only.

Four criteria are employed for performance evaluation by comparing subjective and objective quality measures. Some of the criteria were included in previous tests carried out by the video quality experts group (VQEG) [37]. Other criteria were adopted in previous publications, e.g., [38]. These evaluation criteria are: 1) Spearman rank-order correlation coeffi-

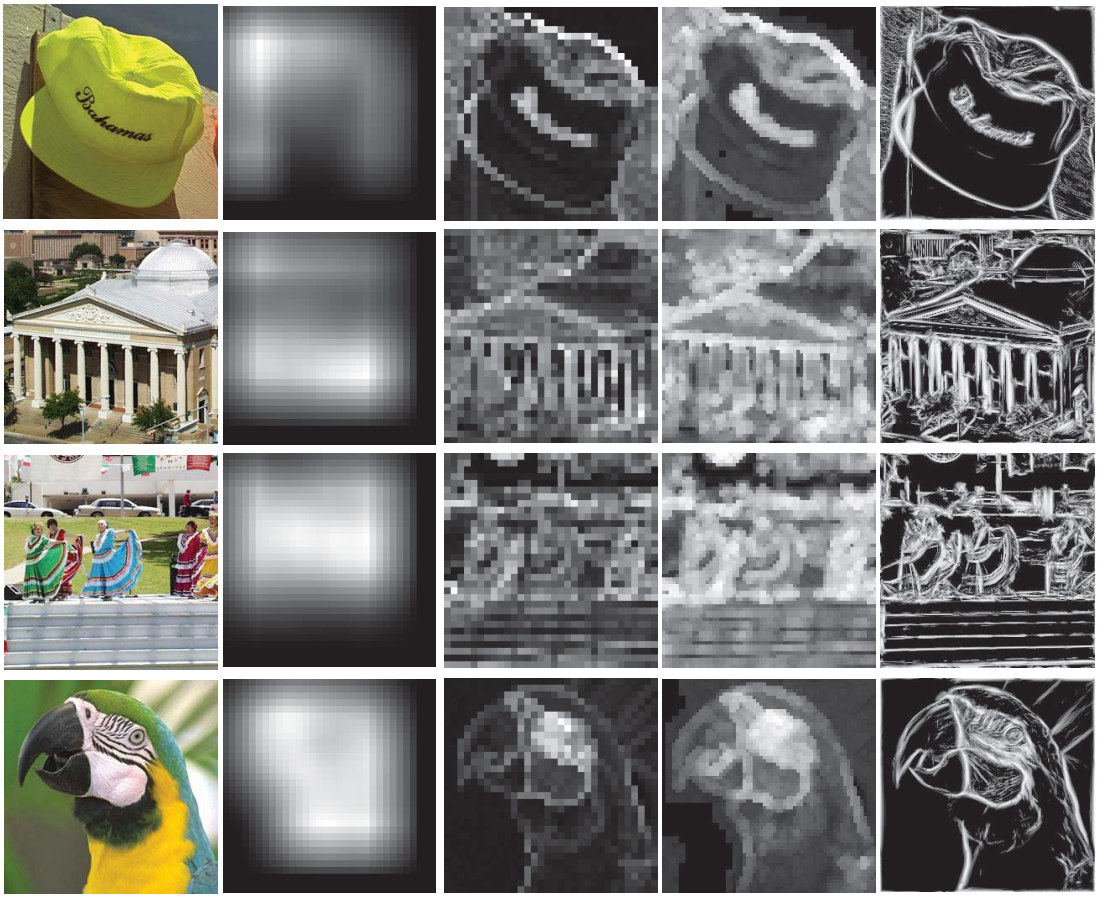

Fig. 4. (a) Sample images and their corresponding (b) CPBD [13], (c) H-metric [18], (d) S_3 [21], and (e) LPC-SI sharpness maps, where brighter indicates higher sharpness.

cient (SRCC); 2) Kendall's rank-order correlation coefficient (KRCC); 3) Pearson linear correlation coefficient (PLCC) after a nonlinear modified logistic mapping between the subjective and objective scores [39]; and 4) root mean squared error (RMSE) between MOS values and model predicted MOS. SRCC and KRCC are both used to assess prediction monotonicity [37]. PLCC and RMSE are employed to evaluate prediction accuracy [37]. A good objective quality measure is expected to achieve high values in PLCC, SRCC and KRCC, and low values in RMSE. In all experiments, only the blurred images in each data set have been included in the computation (i.e., reference images are excluded).

Table IV summarizes the performance comparison results based on all four databases. For each evaluation criterion, we highlight the top two results obtained by NR methods with boldface. To provide an overall evaluation, Table V computes the average PLCC, SRCC and KRCC results for each objective measure over all four databases. The averages are computed using two methods. The first calculates the direct average of the correlation scores over the four databases, and the second computes a weighted average based on the sizes (or the numbers of images) of the image databases (specifically, the weight factors are 145 for LIVE, 100 for TID2008, 150 for CSIQ, and 20 for IVC databases, respectively). The results of both BRISQUE and BLIINDS-II are not included for the LIVE database because they both use LIVE images for training. Subsequently, their average results are computed over the other three databases only. From Tables IV and V, we observe that the proposed LPC-SI measure performs reasonably well and consistently over all four databases and in general are among the most competitive NR methods. Although the comparison is unfair, LPC-SI is often comparable to the FR PSNR, but is inferior to the FR SSIM measure. It is worth mentioning that the good performance of the proposed method is achieved without any edge detection or training processes.

Fig. 3 shows the scatter plots of subjective versus objective quality scores after nonlinear mapping for the four databases, where each sample point represents one test image. The proposed LPC-SI method generally gives reasonable quality predictions, where the sample points tend to be clustered closer to the diagonal lines (representing perfect prediction) than the other five NR methods under comparison. Interestingly, we observe saturation effects of LPC-SI at both low and high quality ends of the scatter plots. The effect is more apparent in LIVE and CSIQ databases, where LPC-SI do not provide further distinctions when the quality of image is beyond or below the saturation levels. Similar effects are also observed in other state-of-the-art sharpness measures such as CPBD [13] and S_3 [21] in case of the CSIQ database. This may be

TABLE IV
PERFORMANCE EVALUATION OVER FOUR DATABASES

LIVE Blur Batabase (145 Images) [29]				
Measure	PLCC	SRCC	KRCC	RMSE
PSNR	0.8782	0.8694	0.6920	13.898
SSIM [2]	0.9997	0.9990	0.9780	0.7416
H-metric [18]	0.7849	0.7147	0.5347	9.7687
Q-metric [19]	0.6971	0.5548	0.4056	11.302
JNBM [11]	0.8130	0.7821	0.6015	9.1797
CPBD [13]	0.9024	0.9271	0.7714	6.7943
S_3 [21]	**0.9494**	**0.9517**	**0.8157**	**4.9503**
BRISQUE [33], [34]	training images			
BLIINDS-II [35], [36]	training images			
LPC-SI	**0.9219**	**0.9501**	**0.7994**	**6.1092**

TID2008 blur database (100 images) [30]				
Measure	PLCC	SRCC	KRCC	RMSE
PSNR	0.8729	0.8702	0.7327	0.5726
SSIM [2]	0.9460	0.9550	0.8147	0.3803
H-metric [18]	0.5144	0.5106	0.3182	1.0063
Q-metric [19]	0.3074	0.3290	0.2208	1.1167
JNBM [11]	0.6931	0.6681	0.4947	0.8459
CPBD [13]	0.8237	0.8418	**0.6297**	0.6655
S_3 [21]	**0.8541**	**0.8418**	0.6124	**0.6103**
BRISQUE [33], [34]	0.8046	0.7989	0.6229	0.6968
BLIINDS-II [35], [36]	0.8260	0.8205	0.6245	0.6614
LPC-SI	**0.8455**	**0.8431**	**0.6249**	**0.6267**

CSIQ blur database (150 images) [31]				
Measure	PLCC	SRCC	KRCC	RMSE
PSNR	0.9252	0.9287	0.7539	0.1087
SSIM [2]	0.9472	0.9605	0.8246	0.0919
H-metric [18]	0.8355	0.7997	0.6274	0.1575
Q-metric [19]	0.7237	0.6528	0.4860	0.1978
JNBM [11]	0.8061	0.7624	0.5971	0.1696
CPBD [13]	0.8822	0.8790	0.6905	0.1349
S_3 [21]	**0.9106**	**0.9058**	**0.7290**	**0.1184**
BRISQUE [33], [34]	**0.9279**	**0.9032**	**0.7353**	**0.1069**
BLIINDS-II [35], [36]	0.8930	0.8765	0.6783	0.1290
LPC-SI	0.9061	0.8931	0.7022	0.1212

IVC blur database (20 images) [32]				
Measure	PLCC	SRCC	KRCC	RMSE
PSNR	0.8883	0.8105	0.6632	0.5243
SSIM [2]	0.9463	0.9353	0.7789	0.3690
H-metric [18]	**0.9423**	**0.9263**	0.7684	**0.3822**
Q-metric [19]	0.9375	**0.9338**	**0.7789**	0.3972
JNBM [11]	0.6983	0.6737	0.4947	0.8172
CPBD [13]	0.8012	0.7744	0.6105	0.6832
S_3 [21]	0.9274	0.8691	0.7090	0.4269
BRISQUE [33], [34]	0.8300	0.8239	0.6561	0.6367
BLIINDS-II [35], [36]	0.7806	0.5262	0.3979	0.7136
LPC-SI	**0.9574**	0.9202	**0.7831**	**0.3295**

due to the facts that image sharpness is not significantly affected with minor image distortions but is completely lost when the distortion is beyond certain level (and thus further distortions do not lead to further degradations of the sharpness measures). This effect also suggests that image sharpness assessment alone may not provide a complete solution to evaluating the quality of blurred images. Other approaches such as naturalness measures may be combined to improve the quality prediction performance.

Statistical significance analysis based on variance-based hypothesis testing provides additional information regarding the relative performance of different image quality models [39]. The assumption behind such analysis is that the residual difference between the subjective score and its prediction by the objective score is Gaussian distributed. In reality, this assumption is not always met perfectly, but is somewhat reasonable because with the large number of sample points, the Central Limit Theorem comes into play and the distribution of the residual difference approximates Gaussian. For a given image database, F-statistic can then be employed to compare the variances of two sets of prediction residuals by two objective methods, so as to determine whether the two sample sets come from the same distribution. As such, we can make a statistically sound judgment regarding superiority or inferiority of one objective method against another. A statistical significance analysis matrix is created and shown in Table VI, where each entry consists of four characters which correspond to the four blur databases in the order of LIVE, TID2008, CSIQ and IVC, respectively. A symbol "$-$" denotes that the two objective methods are statistically indistinguishable, "1" denotes the method of the row is statistically better than that of the column, and "0" denotes that the method of the column is better than that of the row. A symbol "x" denotes unfeasible analysis between row and column method. This is mainly in the case of BRISQUE and BLIINDS-II algorithms over trained data from the LIVE database. It can be observed that S_3 and LPC-SI are statistically indistinguishable for all databases and outperform all other NR sharpness methods for all databases.

One useful feature of the proposed LPC-SI approach is that it provides an LPC map that indicates the spatial variations of local sharpness. Sample images are given in Fig. 4, together with their corresponding sharpness maps produced by CPBD [13], H-Metric [18], S_3 [21] and LPC-SI algorithms. Since the CPBD algorithm requires a large block of size 64 $\times$ 64 [13], to produce more localized measurement,

TABLE V
DIRECT AND WEIGHTED AVERAGE PERFORMANCE OVER FOUR DATABASES

Direct Average			
Measure	PLCC	SRCC	KRCC
PSNR	0.8911	0.8697	0.7105
SSIM [2]	0.9598	0.9625	0.8491
H-metric [18]	0.7693	0.7378	0.5622
Q-metric [19]	0.6664	0.6176	0.4728
JNBM [11]	0.7526	0.7216	0.5470
CPBD [13]	0.8524	0.8556	0.6755
S_3 [21]	**0.9103**	**0.8921**	**0.7165**
BRISQUE [33], [34]	0.8541	0.8420	0.6714
BLIINDS-II [35], [36]	0.8332	0.7411	0.5669
LPC-SI	**0.9077**	**0.9016**	**0.7274**

Database Size-Weighted Average			
Measure	PLCC	SRCC	KRCC
PSNR	0.8944	0.8882	0.7228
SSIM [2]	0.9652	0.9714	0.8736
H-index [18]	0.7456	0.7064	0.5273
Q-index [19]	0.6244	0.5541	0.4081
JNBM [11]	0.7761	0.7423	0.5690
CPBD [13]	0.8713	0.8818	0.7003
S_3 [21]	**0.9113**	**0.9046**	**0.7302**
BRISQUE [33], [34]	0.8749	0.8463	0.6878
BLIINDS-II [35], [36]	0.8598	0.8298	0.6376
LPC-SI	**0.8995**	**0.9023**	**0.7214**

TABLE VI

STATISTICAL SIGNIFICANCE ANALYSIS BASED ON QUALITY PREDICTION RESIDUALS ON LIVE [29], TID2008 [30], CSIQ [31] AND IVC [32] DATABASES

model	PSNR	SSIM	H-Metric	Q-Metric	JNBM	CPBD	LPC-SI	S_3	BRISQUE	BLIINDS2
PSNR	----	000-	-10-	-10-	010-	0-0-	0-00	0-0-	x---	x-0-
SSIM [2]	111-	----	111-	111-	1111	11-1	11--	11--	x111	x111
H-Metric [18]	-01-	000-	----	1-0-	0--1	0001	000-	000-	x011	x011
Q-Metric [19]	-01-	000-	0-1-	----	00-1	0001	000-	000-	x011	x011
JNBM [11]	101-	0000	1--0	11-0	----	000-	0000	000-	x011	x011
CPBD [13]	1-1-	00-0	1110	1110	111-	----	0--0	---0	x-1-	x-1-
LPC-SI	1-11	00--	111-	111-	1111	1--1	----	----	x-11	x-11
S_3 [21]	1-1-	00--	111-	111-	1111	---1	----	----	x-1-	x-11
BRISQUE [33], [34]	x---	x000	x100	x100	x-0-	x-0-	x-00	x-0-	x---	x-0-
BLIINDS-II [35], [36]	x-1-	x000	x100	x100	x10-	x-0-	x-00	x-00	x-1-	x---

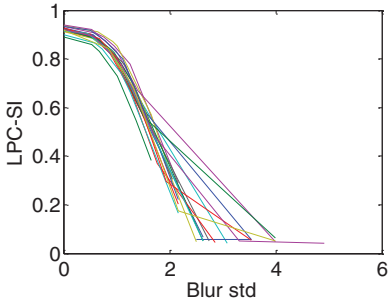

Fig. 5. Relationship between LPC-SI and Gaussian blur standard deviation.

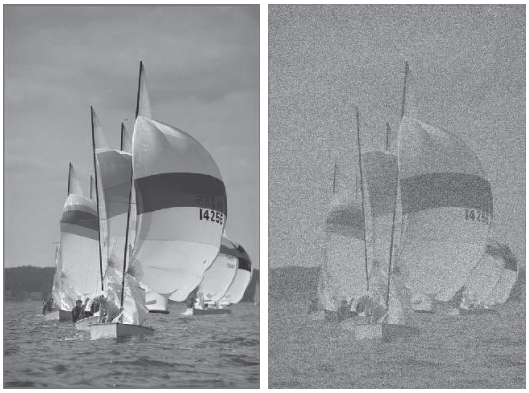

Fig. 6. Example of original and noise corrupted images.

overlapping 64 × 64 windows of step size 8 are used, resulting in blurry sharpness maps, as shown in Fig. 4. The H-metric map is computed by non-overlapping 8 × 8 blocks, and thus creates sharpness maps that have the same resolution but are less burry. S_3 employs different block sizes and overlapping factors for spectral and spatial measurement, and in general further improves the resolution of the sharpness maps. Unlike the other algorithms, LPC-SI does not employ block-based computation, and produces the most localized sharpness map. Visual comparisons of the sample images together with the sharpness maps in Fig. 4 suggest that all four types of sharpness maps convey useful information regarding local sharpness variations, and the H-Metric, S_3 and LPC-SI, to a significant extent, agree with each other, though the localization of the measurement could be very different. It is worth mentioning that these sharpness maps are computed to compare the local behavior of the competing algorithms only, some of which may not be designed to generate accurate local sharpness measurement but to predict the overall human sharpness assessment of the whole image. Moreover, without precise local sharpness assessment by human subjects (which will be our future work), it is difficult to conclude about the relative performance of these maps.

In Fig. 5, we examine the monotonicity between LPC-SI and the numerical level of blur, where Gaussian blur with standard deviation between $\sigma = 0$ and $\sigma = 4$ are tested using source images in the LIVE database. It can be seen that LPC-SI has a monotonic behavior and therefore can successfully rank-order the source image with different blur parameters. On the other hand, the sharpness measures behave differently when blurred images generated from different source images are compared. Similar behavior has also been observed when the same test is applied to the other NR measures in Tables IV and V. It is worth noting that the goal of a perceptual sharpness measure is to predict the perceived blur, but not the numerical factor used to create the blurred image. The perceptual blur and the numerical blur may not perfectly agree with each other, especially when the images are significantly different in texture content and complexity.

Although our algorithm is not designed to work with noise, it is interesting to observe how it reacts when images are contaminated with noise. The impact of noise on perceived sharpness is a complicated issue. Adding noise may (or may not) increase the visual sharpness of flat image regions, but it could significantly affect the perceived sharpness at the sharp edges near an object, which in turn may make it more difficult for the visual system to discern detailed structures in an image. Fig. 6 demonstrates this by showing the "Sail Boats" image that is severely corrupted by noise. In this example, the sharpness of the main objects appear to be weakened by noise. To examine how the proposed method reacts to noise, we plot LPC-SI versus noise level for the "Sail Boats" image in Fig. 7, where we observe that LPC-SI decreases with the increase of noise. We hypothesize that how noise affects perceptual sharpness is content-dependent. It is currently not a conclusive issue and is worth future investigations.

TABLE VII
RUNTIME COMPARISON OF SHARPNESS MEASURES FOR IMAGES OF 1024 × 1024 RESOLUTION

Model	H-metric [18]	JNBM [11]	CPBD [13]	S_3 [21]	BRISQUE [33], [34]	BLIINDS-II [35], [36]	LPC-SI
Runtime (second)	3.86	8.37	11.29	142.5	1.03	572.0	4.37

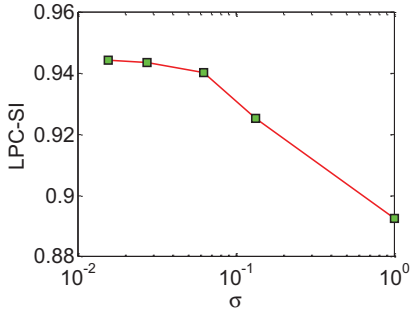

Fig. 7. Relationship between LPC-SI and noise standard deviation σ.

The majority of the computational cost of the proposed LPC-SI algorithm is in the log-Gabor filtering process, which is implemented using the fast Fourier transform (FFT) approach. In the case of L-scale M-orientation filtering, a total of one forward 2-dimensional (2D) FFT and LM inverse 2D-FFTs are performed, and all other computations are linear with respect to the number of pixels N in the image. Therefore, the computational complexity of the proposed algorithm is determined by the complexity of 2D-FFT and is thus in the order of $O(N \log N)$. We have also carried out further experiment to compare the runtime of seven sharpness measures applied on images with 1024 × 1024 resolution. This test was performed using a computer configured with Intel Core i7 CPU at 2.40 GHz, 8 GB RAM, Windows 7 64-bit, and Matalab 7.10. The results are summarized in Table VII, which gives a rough estimate of the relative complexity of the algorithms because the MATLAB code is not optimized for speed. The BRISQUE algorithm requires a long training process but is the fastest in the testing phase among all algorithms being compared. The slowest methods are BLIINDS2 and S_3, both of which involve sophisticated block-based computation. LPC-SI achieves highly competitive perceptual sharpness prediction and is among the fastest algorithms, giving it advantages in real-world applications.

V. CONCLUSION

We propose an LPC-based method for the assessment of perceived image sharpness without referencing the original image. The underlying assumption is that blur affects the LPC relationship near sharp image features and the degradation of LPC strength can be employed to measure image sharpness. We derive a flexible framework to evaluate the LPC strength in arbitrary fractional scales. We propose an efficient algorithm that largely simplifies the LPC computation, making it easily applicable in practical applications. We then develop a novel LPC-SI image sharpness measure, which shows competitive performance when compared with state-of-the-art algorithms. These promising results inspire us to extend the current work to other image processing applications where LPC may be employed as a new type of prior model of sharp natural images.

REFERENCES

[1] Z. Wang and A. C. Bovik, *Modern Image Quality Assessment* (Syntheses Lectures on Image, Video and Multimedia Processing). San Mateo, CA, USA: Morgan & Claypool, 2006.
[2] Z. Wang, A. Bovik, H. Sheikh, and E. Simoncelli, "Image quality assessment: From error visibility to structural similarity," *IEEE Trans. Image Process.*, vol. 13, no. 4, pp. 600–612, Apr. 2004.
[3] H. R. Sheikh and A. C. Bovik, "Image information and visual quality," *IEEE Trans. Image Process.*, vol. 15, no. 2, pp. 430–444, Feb. 2006.
[4] D. Field and N. Brady, "Visual sensitivity, blur and the sources of variability in the amplitude spectra of natural scenes," *Vis. Res.*, vol. 37, no. 23, pp. 3367–3383, Jun. 1997.
[5] L. Firestoneand, K. Cook, N. Talsania, and K. Preston, "Comparison of autofocus methods for automated microscopy," *Cytometry*, vol. 12, no. 3, pp. 195–206, 1991.
[6] N. B. Nill and B. H. Bouzas, "Objective image quality measure derived from digital image power spectra," *Opt. Eng.*, vol. 31, no. 4, pp. 813–825, Apr. 1992.
[7] X. Marichal, W. Ma, and H. J. Zhang, "Blur determination in the compressed domain using DCT information," in *Proc. IEEE Int. Conf. Image Process.*, vol. 2. Oct. 1999, pp. 386–390.
[8] D. Shaked and I. Tastl, "Sharpness measure: Toward automatic image enhancement," in *Proc. IEEE Int. Conf. Image Process.*, vol. 1. Sep. 2005, pp. 937–940.
[9] P. Marziliano, F. Dufaux, S. Winkler, and T. Ebrahimi, "A no-reference perceptual blur metric," in *Proc. IEEE Int. Conf. Process.*, vol. 3. Jun. 2002, pp. 57–60.
[10] E. Ong, W. Lin, Z. Lu, X. Yang, S. Yao, F. Pan, L. Jiang, and F. Moschetti, "A no-reference quality metric for measuring image blur," in *Proc. Int. Symp. Signal Process. Appl.*, vol. 1. Jul. 2003, pp. 469–472.
[11] R. Ferzli and L. Karam, "A no-reference objective image sharpness metric based on the notion of just noticeable blur (JNB)," *IEEE Trans. Image Process.*, vol. 18, no. 4, pp. 717–728, Apr. 2009.
[12] R. Ferzli and L. J. Karam, "Human visual system based on no-reference objective image sharpness metric," in *Proc. IEEE Int. Conf. Image Process.*, Oct. 2006, pp. 2949–2952.
[13] N. Narvekar and L. Karam, "A no-reference image blur metric based on the cumulative probability of blur detection (CPBD)," *IEEE Trans. Image Process.*, vol. 20, no. 9, pp. 2678–2683, Sep. 2011.
[14] S. Erasmus and K. Smith, "An automatic focusing and astigmatism correction system for the SEM and CTEM," *J. Microscopy*, vol. 127, no. 2, pp. 185–199, Aug. 1982.
[15] N. K. Chern, N. P. A. Neow, and M. H. Ang, Jr., "Practical issues in pixel-based autofocusing for machine vision," in *Proc. IEEE Int. Conf. Robot. Autom.*, vol. 3. Jan. 2001, pp. 2791–2796.
[16] J. Caviedes and F. Oberti, "A new sharpness metric based on local kurtosis, edge and energy information," *Signal Process. Image Commun.*, vol. 19, no. 2, pp. 147–161, Feb. 2004.
[17] G. Blanchet, L. Moisan, and B. Rougé, "Measuring the global phase coherence of an image," in *Proc. 15th IEEE Int. Conf. Image Process.*, Oct. 2008, pp. 1176–1179.
[18] X. Zhu and P. Milanfar, "A no-reference sharpness metric sensitive to blur and noise," in *Proc. 1st Int. Workshop Qual. Multimedia Exper.*, Jul. 2009, pp. 64–69.
[19] X. Zhu and P. Milanfar, "Automatic parameter selection for denoising algorithms using a no-reference measure of image content," *IEEE Trans. Image Process.*, vol. 19, no. 12, pp. 3116–3132, Dec. 2010.

[20] Y. Tadmor and D. Tolhurst, "Discrimination of changes in the second-order statistics of natural and synthetic images," *Vis. Res.*, vol. 34, no. 4, pp. 541–554, 1994.
[21] C. Vu, T. Phan, and D. Chandler, "S_3: A spectral and spatial measure of local perceived sharpness in natural images," *IEEE Trans. Image Process.*, vol. 21, no. 3, pp. 934–945, Mar. 2012.
[22] Z. Wang and E. Simoncelli, "Local phase coherence and the perception of blur," in *Advances in Neural Information Processing Systems*, vol. 16. Cambridge, MA, USA: MIT Press, May 2004, pp. 1–8.
[23] P. Kovesi, "Phase congruency: A low-level image invariant," *Psychol. Res.*, vol. 64, no. 2, pp. 136–148, Dec. 2000.
[24] R. Hassen, Z. Wang, and M. Salama, "No-reference image sharpness assessment based on local phase coherence measurement," in *Proc. IEEE Int. Conf. Acoust. Speech Signal Process.*, Mar. 2010, pp. 2434–2437.
[25] R. Hassen, Z. Wang, and M. Salama, "Multi-sensor image registration based-on local phase coherence," in *Proc. 16th IEEE Int. Conf. Image Process.*, Nov. 2009, pp. 181–184.
[26] R. Hassen, Z. Wang, and M. Salama, "Multifocus image fusion using local phase coherence measurement," in *Proc. Int. Conf. Image Anal. Recognit.*, Jul. 2009, pp. 54–63.
[27] E. P. Simoncelli, W. T. Freeman, E. H. Adelson, and D. J. Heeger, "Shiftable multi-scale transforms," *IEEE Trans. Inf. Theory*, vol. 38, no. 2, pp. 587–607, Mar. 1992.
[28] R. Hassen, Z. Wang, and M. Salama, "A flexible framework for local phase coherence computation," in *Proc. Int. Conf. Image Anal. Recognit.*, Jun. 2011, pp. 40–49.
[29] H. Sheikh, Z. Wang, L. Cormack, and A. Bovik. (2007). *LIVE Image Quality Assessment Database Release 2* [Online]. Available: http://live.ece.utexas.edu/research/quality
[30] N. Ponomarenko, V. Lukin, A. Zelensky, K. Egiazarian, M. Carli, and F. Battisti, "TID—A database for evaluation of full-reference visual quality assessment metrics," *Adv. Modern Radioelectron.*, vol. 10, no. 4, pp. 30–45, 2009.
[31] E. Larson and D. Chandler, "Most apparent distortion: Full-reference image quality assessment and the role of strategy," *J. Electron. Imag.*, vol. 19, no. 1, pp. 011006-1–011006-21, Jan. 2010.
[32] P. Le Callet and F. Autrusseau. (2005). *Subjective Quality Assessment IRCCYN/IVC Database 2005* [Online]. Available: http://www.irccyn.ec-nantes.fr/ivcdb/
[33] A. Mittal, A. Moorthy, and A. Bovik, "No-reference image quality assessment in the spatial domain," *IEEE Trans. Image Process.*, vol. 21, no. 12, pp. 4695–4708, Dec. 2012.
[34] A. Mittal, A. K. Moorthy, and A. C. Bovik, "Referenceless image spatial quality evaluation engine," in *Proc. 45th Asilomar Conf. Signals, Syst. Comput.*, Nov. 2011, pp. 1–5.
[35] M. Saad, A. Bovik, and C. Charrier, "Blind image quality assessment: A natural scene statistics approach in the dct domain," *IEEE Trans. Image Process.*, vol. 21, no. 8, pp. 3339–3352, Mar. 2012.
[36] M. Saad, A. Bovik, and C. Charrier, "DCT statistics model-based blind image quality assessment," in *Proc. IEEE Int. Conf. Image Process.*, Sep. 2011, pp. 3093–3096.
[37] *Final Report from the Video Quality Experts Group on the Validation of Objective Models of Video Quality Assessment*. (2000 Mar.) [Online]. Available: http://www.vqeg.org/
[38] Z. Wang and Q. Li, "Information content weighting for perceptual image quality assessment," *IEEE Trans. Image Process.*, vol. 20, no. 5, pp. 1185–1198, May 2010.
[39] H. R. Sheikh, M. F. Sabir, and A. C. Bovik, "A statistical evaluation of recent full reference image quality assessment algorithms," *IEEE Trans. Image Process.*, vol. 15, no. 11, pp. 3440–3451, Nov. 2006.

Rania Hassen received the B.S. and M.Sc. degrees in electrical engineering from Assiut University, Assiut, Egypt, in 2006. She is currently pursuing the Ph.D. degree in electrical and computer engineering with the University of Waterloo, Waterloo, ON, Canada.

Her current research interests include image processing, image quality assessment, medical imaging, and biomedical image processing.

Mrs. Hassen was the recipient of the Ontario Graduate Student Science and Technology Scholarship and the Doctoral Award for Women in Engineering.

Zhou Wang (S'99–A'01–M'02–SM'12) received the Ph.D. degree in electrical and computer engineering from The University of Texas at Austin, TX, USA, in 2001.

He is currently an Associate Professor with the Department of Electrical and Computer Engineering, University of Waterloo, Waterloo, ON, Canada. He has authored more than 100 publications, which received over 10 000 citations (Google Scholar). His current research interests include image processing, coding, and quality assessment; computational vision and pattern analysis; multimedia communications; and biomedical signal processing.

Dr. Wang is a member of the IEEE Multimedia Signal Processing Technical Committee from 2013 to 2015, and an Associate Editor of the IEEE TRANSACTIONS ON IMAGE PROCESSING (2009-Present) and Pattern Recognition (2006-Present). He also served as an Associate Editor of the IEEE Signal Processing Letters from 2006 to 2010, and a Guest Editor of the *IEEE Journal of Selected Topics in Signal Processing* from 2007 to 2009, the *EURASIP Journal of Image and Video Processing* from 2009 to 2010, and Signal, Image and Video Processing from 2011 to 2013. He was a recipient of the 2009 IEEE Signal Processing Society Best Paper Award, the ICIP 2008 IBM Best Student Paper Award (as senior author), and the 2009 Ontario Early Researcher Award.

Magdy M. A. Salama (S'75–M'77–SM'98–F'02) received the B.Sc. and M.S. degrees in electrical engineering from Cairo University, Cairo, Egypt, in 1971 and 1973, respectively, and the Ph.D. degree in electrical engineering from the University of Waterloo, Waterloo, ON, Canada, in 1977.

He is currently a Professor within the Electrical and Computer Engineering Department, University of Waterloo. He has consulted widely with government agencies and the electrical authority. He is a registered Professional Engineer in the Province of Ontario. His current research interests include the operation and control of electric distribution systems and biomedical engineering applications.